

Excitons in hexagonal boron nitride single-layer: a new platform for polaritonics in the ultraviolet

F. Ferreira and A. J. Chaves

Centro de Física and Departamento de Física, Universidade do Minho, Campus de Gualtar, Braga 4710-057, Portugal

N. M. R. Peres and R. M. Ribeiro

*Centro de Física and Departamento de Física and QuantaLab,
Universidade do Minho, Campus de Gualtar, Braga 4710-057, Portugal and
International Iberian Nanotechnology Laboratory (INL),
Av. Mestre José Veiga, 4715-330 Braga, Portugal*

(Dated: July 18, 2018)

The electronic and optical properties of 2D hexagonal boron nitride are studied using first principle calculations. GW and BSE methods are employed in order to predict with better accuracy the excited and excitonic properties of this material. We determine the values of the band gap, optical gap, excitonic binding energies and analyse the excitonic wave functions. We also calculate the exciton energies following an equation of motion formalism and the Elliot formula, and find a very good agreement with the $GW+BSE$ method. The optical properties are studied for both the TM and TE modes, showing that 2D hBN is a good candidate to polaritonics in the UV range. In particular it is shown that a single layer of h-BN can act as an almost perfect mirror for ultraviolet electromagnetic radiation.

I. INTRODUCTION

Two dimensional hexagonal boron nitride (hBN), also called by some white graphene, is an electrical insulator in which the boron (B) and nitrogen (N) atoms are arranged in a honeycomb lattice and are bounded by strong covalent bonds. Like graphene, hBN has good mechanical properties¹ and high thermal conductivity.² Specially interesting is the possibility of using hBN as a buffer layer in van der Waals heterostructures, namely ones comprised by layers of h-BN/graphene.³ Hexagonal boron nitride layer can serve as a dielectric or a substrate material for graphene in order to improve its mobility⁴ and open a gap⁵. It can also be used to improve the thermoelectric performance of graphene.⁶

Yet, its electronic properties differ significantly from graphene. Graphene π and π^* electronic bands have a linear dispersion at the K point, whereas in hBN there is a lift of the degeneracy at the same point and a wide band gap greater than 7 eV is formed, at least within an independent electron picture. That would, in principle, make it ideal for optoelectronic devices in the deep ultraviolet region^{7,8}. As we will see, however, excitonic effects play an important role in this material: excitonic peaks are created at the near UV, and this is a much more useful electromagnetic spectral range, when compared to the deep UV.

The optical properties of monolayer hBN at the UV range are characterized by the exciton with a corresponding optical band gap calculated in the range 5.30–6.30 eV (see Sec. II). The presence of the exciton in this range can be used to excite exciton-polaritons, that share some properties with surface plasmon-polaritons^{9,10}. Therefore, the UV optical properties of hBN can be used as an alternative to the emerging field of UV plasmonics.^{11–20} The plasmonics in UV range also attracts interest in

biological tissue²¹ as consequence of the resonances in nucleotide bases and aromatic amino acids. Plasmonics in this ranges relies in poor metals^{13,15,16,22} and Rhodium^{17,18,20}.

Because of the difficulty of its synthesis, few experimental works have been done for hBN single layer. Also, to study and probe its electronic and optical properties it is necessary to work in UV range. To our best knowledge only one experimental work²³ has been produced that studies the electronic properties of 2D hBN. Those authors observed the band structure of BN monolayer on Ni(111) surface by using angle-resolved ultraviolet-photoelectron spectroscopy and angle-resolved secondary-electron-emission spectroscopy. Because the bond between the interface of h-BN and Ni(111) is weak, the band-structure observed can be regarded as that of the monolayer h-BN. The band gap was determined to be ~ 7 eV and after a comparison with theoretical works, the authors conclude that the band gap is estimated to be within the range of 4.6 to 7.0 eV, too wide when compared with numerical results. These theoretical works were based on first principles calculations using Density Functional Theory (DFT). It is well known that DFT does not predict with good accuracy the electronic and optical properties of semiconductors and insulators. Accurate values require a theory that include many-body effects like the GW approximation.^{24,25} To obtain optical properties, a theory that includes the excitonic properties is also needed. Usually, the Bethe-Salpeter equation (BSE)^{26,27} is used.

There are several works in the literature that used the GW approximation^{28–30} and $GW+BSE$ ^{31–33} on 2D h-BN. The results from these works vary significantly, as can be seen in Table I. There is no agreement even on whether the gap is direct or indirect. Convergence can be an issue in GW and BSE calculations as can be seen

in References 34 and 35. It is likely that the works summarized in Table I use different criteria for convergence and that may explain the differences.

A small number of bands used in the calculation^{28,29} or not using a truncation to avoid interaction with periodic images³⁰ may also explain some differences. Sometimes there is some ambiguity between the value stated for the gap and the one that can be obtained from the absorption spectrum presented.³² More difficult to explain are the values obtained in Ref. 33. They differ significantly from our work and others, although they seem to have converged the calculations carefully. One explanation may be that they fixed the lattice constant at the experimental value, instead of relaxing the unit cell. The experimental lattice constant may not match the value that actually optimizes the system and can influence the values of the gaps in the electronic band-structure. An effective-energy technique³⁶ was adopted in Ref. 31. That technique allowed the calculation of the screened Coulomb interaction W to be converged with only 90 bands and 60 bands for the self-energy Σ calculation. The use of such technique certainly will produce some differences in the final results.

In this work we clarify whether the gap in hBN is direct or indirect, as well as their values and the exciton energies. We also calculate the excitonic spectra using an equation of motion formalism and the Elliot formula, fitting it with the $GW+BSE$ calculations thus obtaining a validation of the method. In Section II we describe the details of the G_0W_0 calculations and results. In Section III we show the results of the BSE calculations. Both G_0W_0 and BSE calculations were performed with the software package BERKELEYGW.³⁷⁻³⁹ Section IV presents the equation of motion formalism and the results for the excitonic properties of monolayer hBN. In Section V we study the properties of exciton-polaritons of hBN and we show that a monolayer of hBN can be used as a UV mirror. We finally draw the conclusions in Section VI.

Table I. Several band gaps calculated in this work and by other authors using GW_0 , G_0W_0 and BSE, in eV. K \rightarrow K indicates the direct gap at the K point, K \rightarrow Γ indicates the indirect gap from the K to the Γ point, O. Gap is the optical gap and EBE the excitonic binding energy.

Reference	Calculation	K \rightarrow K	K \rightarrow Γ	O. Gap	EBE
This work	$G_0W_0 + BSE$	7.77	7.32	5.58	2.19
Ref. 32	$GW_0 + BSE$	7.80	-	6.30	2.10 or 1.50
Ref. 31	$G_0W_0 + BSE$	7.36	-	5.30	2.06
Ref. 33	$G_0W_0 + BSE$	7.25	-	-	1.90
Ref. 30	G_0W_0	-	7.40	-	-
Ref. 29	GW_0	-	6.86	-	-
Ref. 28	G_0W_0	-	6.00	-	-

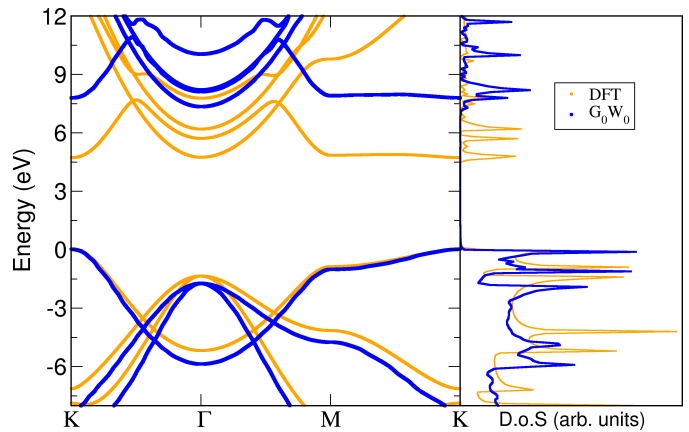


Figure 1. (Color online) Electronic band structure (left) and electronic density of states of h-BN (right) for both DFT and GW calculations.

II. G_0W_0 RESULTS

G_0W_0 calculations were done on top of DFT calculations with a scalar-relativistic norm-conserving pseudopotential. The software package QUANTUM ESPRESSO⁴⁰ was used for the DFT calculations. The details of the DFT calculations are summarized in Table II. For G_0W_0 calculations, a truncation technique is needed due to the non-local nature of this theory.

We found that for DFT calculations a grid of $6 \times 6 \times 1$ \mathbf{k} -points is enough to reach convergence. For the GW calculations, a grid of $16 \times 16 \times 1$ \mathbf{k} -points and a cut off energy of 22.6 Ry and 1100 bands were needed for the dielectric matrix calculations. For the Σ self-energy calculation we used a cut off energy of 22.6 Ry and 1000 bands. The results obtained for the electronic band gap are summarized in Table III. They show that a monolayer of hBN is a wide band-gap indirect-gap material. Fig. 1 presents the electronic band structure and electronic density of states for both DFT and GW calculations.

As mentioned in the Introduction, the only experimental work we are aware of is the one from Ref. 23, which in fact estimates the band gap based on theoretical works that used mean field calculations to predict the electronic properties of bulk h-BN. Mean field theories such as DFT underestimate the band gap value of semiconductors and insulator materials. They obtain a wide range of possible values, from 4.6 to 7.0 eV. We believe that a value closer to 7.0 eV is more reliable, since the gap value for the

Table II. Details of DFT calculations.

Exchange-correlation functional	GGA-PBE ⁴¹
Plane-wave cut-off	70 Ry
\mathbf{K} -point sampling (Monkhorst-Pack) ⁴²	$6 \times 6 \times 1$
Interlayer distance	15.8 Å
Lattice constant	2.5 Å

Table III. G_0W_0 gap values for the transitions $K \rightarrow \Gamma$, $K \rightarrow K$ and $\Gamma \rightarrow \Gamma$, and optical gap and exciton binding energy (EBE) obtained from BSE in this work. The results show that hBN is an indirect-gap insulator.

Transition	$K \rightarrow \Gamma$	$K \rightarrow K$	$\Gamma \rightarrow \Gamma$	Optical	EBE
Energy [eV]	7.32	7.77	9.07	5.58	2.19

bulk materials are lower when compared to the monolayer counterpart. And is actually closer to the ones obtained by works referred in Table I. Still, more experimental work is needed.

Ref. 23 also calculated the width of the valence bands, and they found no good agreement with theoretical works of the time. Table IV shows the width of the valence bands as calculated with DFT, GW and the experimental determination of Ref. 23. The π -band is the one that has its highest energy at the K-point, while the σ_1 and σ_2 are the bands that have the highest energy at the Γ point. Table IV shows that DFT results differ from the experimental ones by values greater than 0.5 eV in all cases. On the other hand, G_0W_0 results differ from the experimental results by values equal or smaller than 0.1 eV.

We also calculated the effective masses of the highest valence band and lowest conduction band using both G_0W_0 and DFT (Table V). We found no differences between G_0W_0 and DFT, except for the effective mass at $K \rightarrow \Gamma$ on the first conduction band (DFT value greater by $0.08m_e$). Thus we conclude that DFT calculations are reliable to obtain the values of the effective masses in this material.

Ref. 28 also calculated the effective mass at the Γ point for the conduction band, and obtained a value of $(0.95 \pm 0.05)m_e$ with only slight variations for different planar directions. In our work we obtained differences of $0.3m_e$ between different directions in reciprocal space at the Γ point.

III. BSE RESULTS

After determining the conduction and valence band states, the electron-hole pair states are determined using the Bethe-Salpeter (BSE) equation. The imaginary

Table IV. Width of the valence bands. π band is the top valence band at K point. σ_1 and σ_2 are the bands that have the highest energy at the Γ point. The difference is in the width of the bands which is greater for σ_2 .

Width of bands [eV]	π band	σ_1 band	σ_2 band
This work (DFT)	5.20	5.78	7.49
This work (G_0W_0)	5.90	6.42	8.24
Experimental ²³	5.80	6.50	8.20

Table V. Effective masses (in electron mass (m_e) units) for hBN calculated using G_0W_0 . The arrow indicate the direction in which the effective mass is calculated.

Symmetry points	Effective mass m^*/m_e			
	$K \rightarrow \Gamma$	$\Gamma \rightarrow K$	$\Gamma \rightarrow M$	$M \rightarrow \Gamma$
Valence band	0.63	0.82	1.09	0.46
Conduction band	0.83	0.95	1.27	0.35

part of the dielectric function $\epsilon_2(\omega)$ is then³⁹

$$\epsilon_2(\omega) = \frac{8\pi^2 e^2}{\omega^2} \sum_S |\mathbf{e} \cdot \langle 0 | \mathbf{v} | S \rangle|^2 \delta(\omega - \Omega^S) \quad (1)$$

where Ω^S is the energy for an excitonic state S , $\langle 0 | \mathbf{v} | S \rangle$ is the velocity matrix element, and \mathbf{e} is the direction of the polarization of incident light with energy ω . e is the electron charge.

If we do not consider excitonic effects, the expression becomes a transition between single particle states³⁹

$$\epsilon_2(\omega) = \frac{8\pi^2 e^2}{\omega^2} \sum_{v\mathbf{k}} |\mathbf{e} \cdot \langle v\mathbf{k} | \mathbf{v} | c\mathbf{k} \rangle|^2 \delta(\omega - (E_{c\mathbf{k}} - E_{v\mathbf{k}})) \quad (2)$$

which is a random phase approximation (RPA). The labels v (c) denotes valence (conduction) band states, and \mathbf{k} denotes the single particle momentum (only vertical transitions are considered).

Fig. 2 shows the imaginary part of the dielectric function calculated by BSE, done on top of a G_0W_0 calculation with a grid of $16 \times 16 \times 1$ \mathbf{k} -points. The convergence of the G_0W_0 band structure with a particular grid of \mathbf{k} -points does not imply that BSE will be converged with the same grid. An interpolation with a fine grid of $120 \times 120 \times 1$ \mathbf{k} -points was needed to achieve convergence. Fig. 2 also shows the imaginary part of dielectric function without excitonic effects. The first peak has an energy of 5.58 eV and the second peak has an energy of 6.48 eV. In Table III we summarize the gap values of the band structure, the optical gap and the excitonic binding energy. Fig. 3 shows the real part of the dielectric function calculated with and without excitonic effects.

We also calculated the eigenvalues of the two particle states. Figure 4 shows the energies of the 8 lowest energy excitonic states. From now we label each state by the corresponding energy in an ascending order. The pairs of states (1,2), (3,4), and (7,8) are degenerate. States 1 and 2 are the degenerated ground state. We plot the probability density $|\phi(\mathbf{r}_e, \mathbf{r}_h)|^2$ obtained from the BSE for these eight excitonic states in Fig. 5. These plots show the probability to find an electron at position \mathbf{r}_e if the hole is located at \mathbf{r}_h . We set the hole localized slightly above the nitrogen atom. The results were calculated using a coarse grid of $12 \times 12 \times 1$ \mathbf{k} -points and a BSE interpolation of $72 \times 72 \times 1$ \mathbf{k} -points. It can be noticed the complementarity of the degenerate states. For instance,

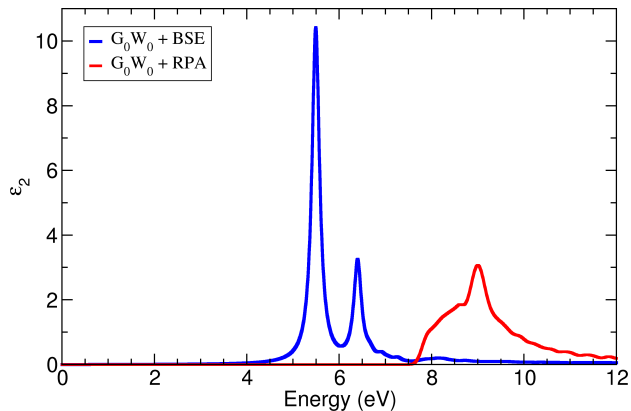


Figure 2. (Color online) Imaginary part of dielectric function of 2D h-BN. The blue (red) lines represent the BSE (RPA) imaginary part of dielectric function.

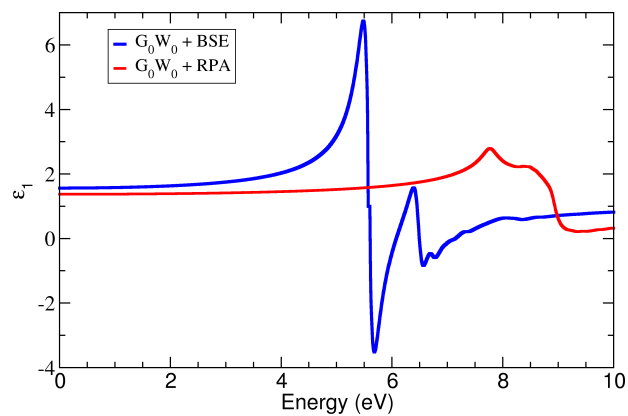


Figure 3. (Color online) Real part of the dielectric function of 2D h-BN. The blue (red) lines represent the BSE (RPA) real part of dielectric function.

if one adds the probability density of states 3 and 4, the symmetry of the lattice is recovered. And the same can be seen for the other degenerate states. The work of Ref. 33 has also studied the excitonic states. Their results are in good agreement with the ones obtained from this work.

IV. BSE IN THE EQUATION OF MOTION FORMALISM AND THE ELLIOT FORMULA

In this section we will follow the approach of the equation of motion derived in Ref. 43 and detailed in the Appendix A. The formalism is grounded on the calculation of the expected value of the polarization operator $\hat{P}(t)$ after we introduce an external electric field of intensity \mathcal{E}_0 and frequency ω that couples with the electron gas in the 2D material. The optical conductivity and other properties can be obtained from the macroscopic relations. The starting point of our model is an effective Dirac hamiltonian,⁴⁴ that can be obtained from a power

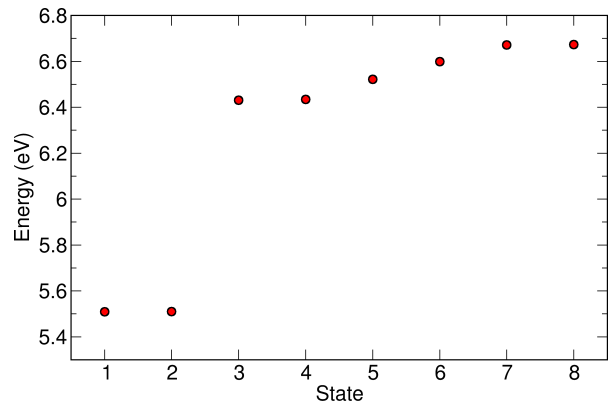


Figure 4. (Color online) Excitonic energies for the lowest energy exciton states. The system has a C_{3v} symmetry with three representations: A_1 , E and A_2 . The states 1 to 4 have E symmetry and are valley degenerate; states 5 and 6 have A_2 and A_1 symmetries respectively and are non degenerate (see Ref. 33).

series expansion of the tight-binding hamiltonian. The electron-electron interaction for a 2D material is given by the Keldysh potential.⁴⁵ This effective model only considers the top valence band and the bottom conduction band.

From the equation of motion we derive the following BSE:

$$(\omega - \tilde{\omega}_{\lambda\mathbf{k}}) p_{\lambda}(\mathbf{k}, \omega) = (\mathcal{E}_0 d_{\lambda}(\mathbf{k}) + \mathcal{B}_{\mathbf{k}\lambda}(\omega)) \Delta f_{\mathbf{k}}, \quad (3)$$

where $\lambda = \pm$, $p_{\pm}(\mathbf{k}, \omega)$ is the interband transition amplitude, $\tilde{\omega}_{\lambda\mathbf{k}}$ is the transition energy renormalized by the exchange self-energy and $\mathcal{B}_{\mathbf{k}\lambda}(\omega)$ is a term that renormalizes the Rabi-Frequency, $d_{\lambda}(k)$ is the dipole matrix element and $\Delta f_{\mathbf{k}}$ is the occupation difference, given by the Fermi-Dirac distribution. See Appendix A for more details.

From the homogeneous part of Eq. (3) we can obtain the exciton energies and the wave functions. Using the procedure explained in Ref. 43, we can obtain the corresponding Elliot formula for the optical conductivity:

$$\frac{\sigma(\omega)}{\sigma_0} = 4i\hbar\omega \sum_n \frac{p_n}{\hbar\omega - E_n + i\gamma}, \quad (4)$$

where n labels the exciton state, γ is the exciton linewidth, E_n the exciton energy, p_n the corresponding exciton weight and $\sigma_0 = \frac{e^2}{4\hbar}$. Fig. 6 shows that the G_0W_0 +BSE described in section III fits well to the Elliot formula, with a very good agreement in the real part and a small shift in the imaginary part. The energies and weights of the fit for the G_0W_0 +BSE and the equation of motion method are compared in table VI. We use the parameters from Ref. 44: $a_0 = 2.51 \text{ \AA}$, $t_0 = 2.33 \text{ eV}$ $\hbar v_F = \frac{\sqrt{3}}{2} t_0 a_0$, $2mv_F^2 = 3.92 \text{ eV}$. The Keldysh potential parameter r_0 was calculated in Ref. 33 to be $r_0 = 10 \text{ \AA}$. We can see an excellent agreement between the exciton energies of both methods. The difference in the weights p_n

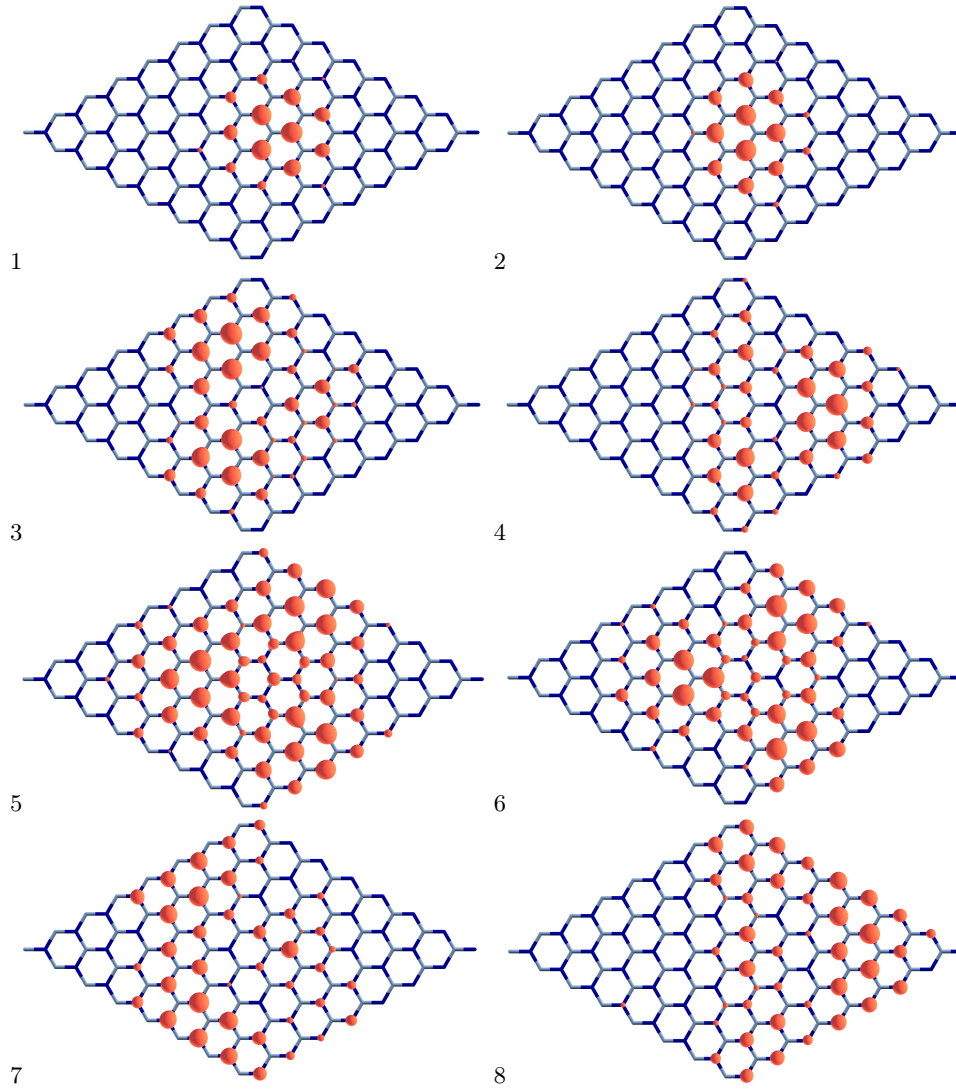


Figure 5. (Color online) Probability density $|\phi(\mathbf{r}_e, \mathbf{r}_h)|^2$ for the exciton states 1 to 8. The hole is localized slightly above the nitrogen atom (light color) at the centre of the lattice.

can be explained by the oversimplification of the Dirac hamiltonian used for the Elliot formula and consequently the less accurate dipole matrix elements that enter their calculation.

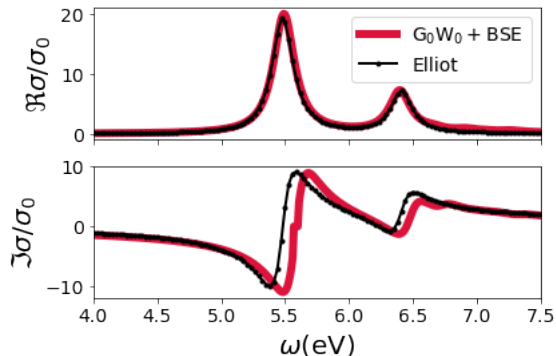


Figure 6. (Color online) Fit of the Elliot formula to the G_0W_0+BSE result. There is a very good agreement for the real part and a small shift in the imaginary part; the exciton linewidth used was $\gamma = 0.1$ eV. The parameters of the fitting are shown in table VI.

Finally, we used the equation of motion to predict the behavior of the exciton energy and the $K \rightarrow K$ transition energy as a function of the environment dielectric constant. The result can be seen in Fig. 7. There is a strong decrease in the $K \rightarrow K$ transition energy and an almost linear behavior, also decreasing, of the first exciton energy as the external dielectric constant increases. This effect is simple to understand, since a large dielectric constant screens more effectively the electron-electron interaction.

V. EXCITON-POLARITONS

In this section we discuss the exciton-polariton modes in 2D hBN. Those modes are electromagnetic evanescent waves along the direction perpendicular to the hBN sheet. We assume that the hBN monolayer is cladded between two uniform, isotropic media with dielectric constants ε_1 and ε_2 and that the hBN sheet is in the xy -plane. So the electromagnetic mode is evanescent in the z axis and proportional to $e^{-\kappa_i z}$ ($i = 1, 2$). The modes can be classified as transverse magnetic or transverse electric (TM/TE).

Table VI. Comparison of the Elliot formula parameters used in the G_0W_0+BSE calculation and the equation of motion approach. The spin and valley degeneracy is already included in the weight.

	E_1 (eV)	p_1	E_2 (eV)	p_2
G_0W_0+BSE	5.48	0.088	6.41	0.027
Eq. of Motion	5.52	0.354	6.53	0.045

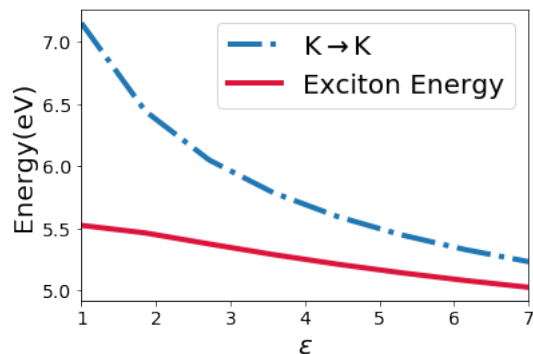


Figure 7. (Color online) Exciton and $K \rightarrow K$ transition energy as function of the environment dielectric constant. We can see that the dependence of the first exciton energy is almost linear while the $K \rightarrow K$ transition energy has a greater dependence on the dielectric constant.

The dispersion relation for the TM mode is given by the solution given in Ref. 46:

$$\frac{\varepsilon_1}{\kappa_1} + \frac{\varepsilon_2}{\kappa_2} + i \frac{\sigma(\omega)}{\varepsilon_0 \omega} = 0, \quad (5)$$

and for the TE mode:

$$\kappa_1 + \kappa_2 - i \omega \mu_0 \sigma(\omega) = 0, \quad (6)$$

with $\sigma(\omega)$ the hBN optical conductivity and:

$$\kappa_i = \sqrt{q^2 - \varepsilon_i \frac{\omega^2}{c^2}}, \quad (7)$$

where q is the exciton-polariton in-plane wavevector and c is the velocity of light in vacuum. We shall consider the simplest case of $\varepsilon_1 = \varepsilon_2 = 1$. A rule of thumb is that when $\Im \sigma(\omega) > 0$ ($\Im \sigma(\omega) < 0$) TM (TE) modes are supported.

A. Complex $q \times$ Complex ω

First, we note that both Eqs. (5) and (6) are complex. Therefore, for a given q (ω) real, the solution will be a complex ω (q). Each of these approaches (complex q or complex ω) lead to different dispersion relations for the exciton-polaritons as discussed elsewhere.⁴⁷⁻⁵¹ Both complex q and complex ω approaches give the same results when an active media is used to balance the losses.⁵¹ The complex q approach is suitable when the polariton is excited in a finite region of space with a monochromatic wave, while the complex ω approach is valid instead when the entire sample is excited by a pulsed light.⁴⁹

The dispersion relation for both the TE and TM modes in the complex ω approach was obtained by solving Eqs. (5) and (6) and using the Elliot formula (4) with the parameters of table (VI) for the G_0W_0+BSE calculation and a damping of $\gamma = 0.1$ eV. The result is shown in

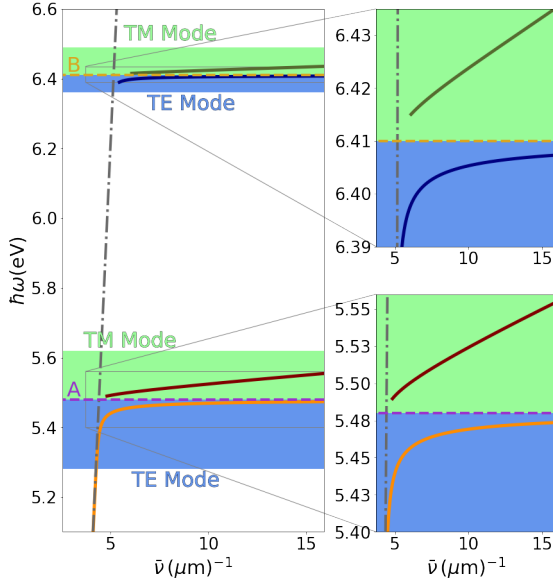


Figure 8. (Color online) Exciton-polariton dispersion relation for complex frequency. The results are given as a function of the wavenumber $\bar{\nu} = \lambda_q^{-1}$. The gray dashed-dotted line represents the light cone in air. In this approach, the wavenumber can reach large values for both TE and TM modes for either A or B exciton energies. Detail around excitons A and B is shown in the right panels.

Fig. 8, where A and B denote the first two excitonic energies. Both TE and TM modes can have a large localization (high κ_i or q) in this case. The TE mode has a flat dispersion relation that approaches the exciton energy as q goes to infinity. As expected, the TM mode has a higher frequency than the exciton energy while the TE mode has a lower frequency. We point out that, and contrary to graphene, the TE mode presents a high degree of localization.

In the complex ω approach both excitons A and B support polaritons. This can be understood by examining Eq. (4). As $\hbar\omega$ approaches $E_n - i\gamma$, the corresponding contribution to the optical conductivity diverges. This quantity can be infinitely negative or positive depending on the real part of the frequency approaching E_n from the right or the left, supporting TM and TE modes respectively. Fig. 8 also shows that the electrostatic limit $q \gg \omega/c$ is approached near both exciton energies. In that limit the lifetime τ of the TM exciton-polariton $\tau = -1/\Im\omega$ can be calculated from (see Appendix B):

$$\tau^{-1} = \frac{\gamma}{\hbar} + \frac{1}{\hbar} \frac{p_n \Im[b_n]}{\left| \frac{(\varepsilon_1 + \varepsilon_2)b_n}{4\pi\alpha c q} + 1 \right|^2}, \quad (8)$$

where α is the fine-structure constant and b_n is the contribution that arises from the background conductivity provenient from interband transitions and other excitonic states. For a negligible background $b_n \approx 0$, the exciton-polariton lifetime is proportional to the inverse of the

exciton linewidth γ .

Next we shall consider the case of complex q . There will be then a simple relation to obtain q for a given frequency (assuming $\varepsilon_i = 1$):

$$c^2 q^2 = \omega^2 + c^2 \kappa_\alpha^2(\omega), \quad (9)$$

with $\alpha = \text{TM/TE}$ and from Eqs. (5) and (6) we have:

$$\kappa_{\text{TE}}(\omega) = i \frac{\varepsilon_0 \omega}{2\sigma(\omega)}, \quad (10a)$$

$$\kappa_{\text{TM}}(\omega) = i \frac{\omega \mu_0 \sigma(\omega)}{2}, \quad (10b)$$

The condition for the existence of polaritons is $\Re \kappa_\alpha > 0$. These equations allowed us to calculate the dispersion relation shown in Fig. 9 for several values of the damping constant γ . The dependence of the γ parameter of excitons was studied for WS_2 in Ref.⁵² as function of temperature, showing that the linewidth decreases as the temperature decreases. From Fig. 9 we can see that the TE mode is strongly suppressed except when the damping has the very low value of 4 meV, close to the intrinsic line-width. The opposite happens for the TM mode, for which the dispersion relation is almost insensitive to the damping γ .

An important figure of merit is the ratio of the propagation length $\ell = \Im q^{-1}$ to the exciton wavelength $\lambda_q = 2\pi/\Re q$, as it indicates if a polariton can propagate before extinction, that is shown in Fig. 10 for several values of γ . The TM mode is highly suppressed except for the very low $\gamma = 4$ meV, while the TE mode has higher propagation rate and two different qualitative behaviors. For larger γ , the propagation rate increases with the frequency while the opposite happens for $\gamma = 4$ meV. A better understanding of this behavior can be achieved if we consider the confinement ratio λ_0/λ_q , with λ_0 being the wavelength of the free-radiation (see Figure 11). The confinement of the TM modes increases with increasing frequency and have a negligible γ dependence. On the other hand, the TE modes are poorly confined, with the confinement going to zero faster with increasing γ . This explains the large propagation rate in this case: the poorly confined field is essentially attenuated free radiation, i.e., there are no more excitons being excited, but the radiation field is attenuated by the material free charges.

The overall conclusion is that 2D hBN is a good platform for exciton-polaritons when we consider the complex ω approach for both TM and TE modes. In the complex q approach, the results show that exciton-polariton can be observed only for $\gamma = 4$ meV.

B. UV radiation mirror

It was pointed out recently that excitons in MoSe_2 can lead to very high reflection of electromagnetic radiation^{53,54}. In this section we show that the same

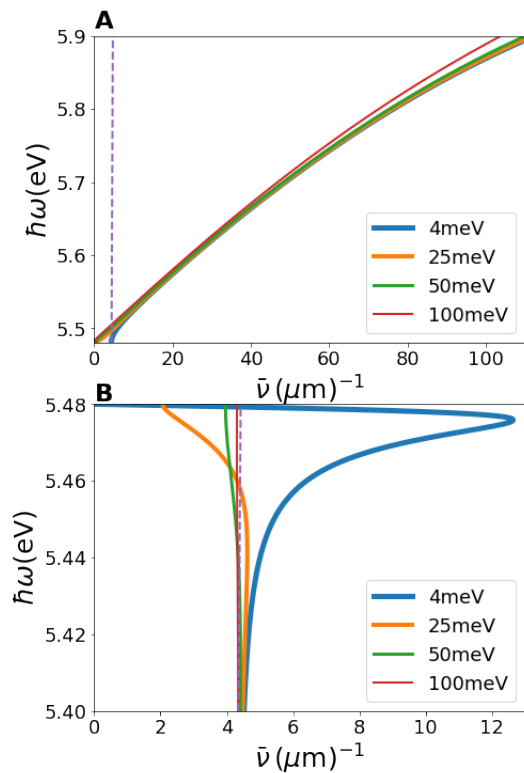


Figure 9. (Color online) Exciton-polariton dispersion relation in the complex wavenumber approach. Panel A (B) shows the TM (TE) mode. The TM mode has a dispersion almost insensitive to the relaxation rate while the TE mode changes significantly: the wavenumber is close to the free-light one and only for $\gamma = 4$ meV there is a different behavior.

occurs with hBN, but in a different spectral range. We consider a free-standing hBN monolayer. In this case the reflection is given by:⁵⁵

$$\mathcal{R} = \left| \frac{\pi\alpha f(\omega)}{2 + \pi\alpha f(\omega)} \right|^2, \quad (11)$$

where $f(\omega) = \sigma(\omega)/\sigma_0$, $\alpha \approx 137^{-1}$ is the fine structure constant and $\sigma_0 = e^2/4\hbar$. Fig. 12 shows that the reflection can reach almost 100% for the value $\gamma = 4$ meV at the *A* exciton energy. This is a consequence of the very high weights for hBN that appears in the Elliot formula (see table VI). We emphasize that those results are for a free-standing hBN sheet. The γ value can be controlled by the temperature as discussed in the sections before. As shown in Fig. 7, the exciton energy and therefore the reflection peak can be controlled by varying the external dielectric constant.

VI. CONCLUSION

We calculated the band structure of 2D hexagonal boron nitride using DFT and the G_0W_0 approximation.

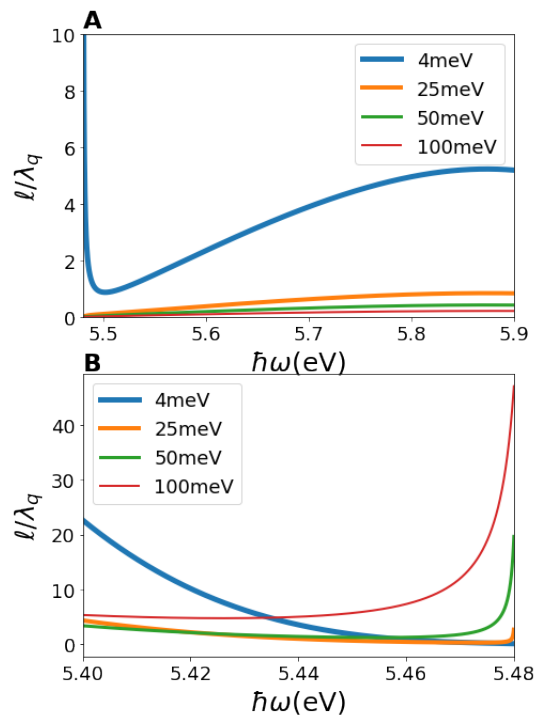


Figure 10. (Color online) Exciton-polariton propagation ratio. Panel A (B) shows the TM (TE) mode. The propagation rate of the TM mode is very low except for $\gamma = 4$ meV. The peak at $\omega = 5.48$ corresponds to the propagation of radiation. As can be seen in Fig. 9, the wavenumber tends to the free-light wavenumber. The same result appears in the propagation rate for the TE modes: except for $\gamma = 4$ meV, all other modes correspond to poorly confined modes (see Fig. 11 also). For $\gamma = 4$ meV and the TE mode, the propagation rate decreases with the increasing frequency.

Then the Bethe-Salpeter equation was used to determine the excitonic energies of hBN. We determined the values of the band gap, optical gap, excitonic binding energies using a first principles approach. The results are in very good agreement with the ones obtained using a very different approach, namely the equation of motion formalism and the Elliot formula, which are also presented in this paper. This latter formalism allowed us to study the optical properties for both the TM and TE modes. Our results show that 2D hBN is a good candidate to polaritonics in the UV range. We also show that a single layer h-BN can act as an almost perfect mirror for ultraviolet electromagnetic radiation.

ACKNOWLEDGMENTS

R.M.R. and N.M.R.P. acknowledge support from the European Commission through the project “Graphene-Driven Revolutions in ICT and Beyond” (Ref. No. 785219), COMPETE2020, PORTUGAL2020, FEDER and the Portuguese Foundation for Science and Technol-

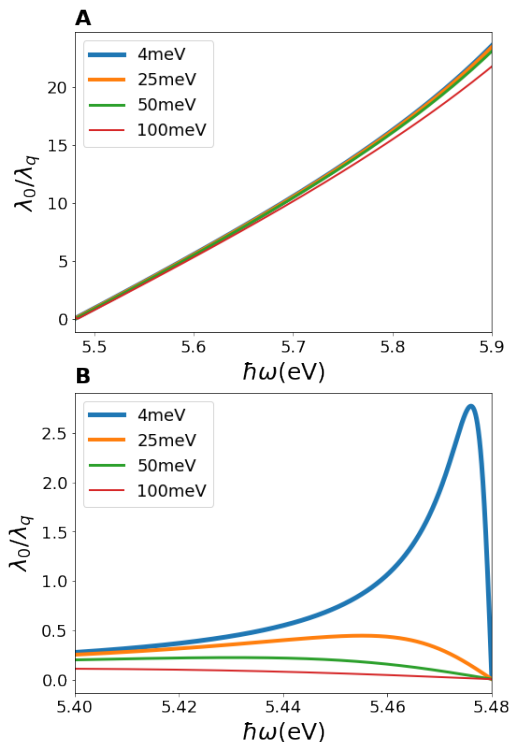


Figure 11. (Color online) Exciton-polariton confinement ratio. Panel A (B) shows the TM (TE) mode. The confinement of the TM mode increases with the frequency and has a small dependence with the relaxation rate γ . The TE modes for the higher values of γ are poorly confined. For the value $\gamma = 4$ meV we have a peak in the confinement below the exciton energy.

ogy (FCT) through project PTDC/FIS-NAN/3668/2014 and in the framework of the Strategic Financing UID/FIS/04650/2013.

- ¹ J. Bao, K. Jeppson, M. Edwards, Y. Fu, L. Ye, X. Lu, and J. Liu, *Electronic Materials Letters* **12**, 1 (2016).
- ² J. Bao, M. Edwards, S. Huang, Y. Zhang, Y. Fu, X. Lu, Z. Yuan, K. Jeppson, and J. Liu, *Journal of Physics D: Applied Physics* **49**, 265501 (2016).
- ³ B. Amorim, R. M. Ribeiro, and N. M. R. Peres, *Phys. Rev. B* **93**, 235403 (2016).
- ⁴ L. Banszerus, M. Schmitz, S. Engels, M. Goldsche, K. Watanabe, T. Taniguchi, B. Beschoten, and C. Stampfer, *Nano Letters* **16**, 1387 (2016), pMID: 26761190, <http://dx.doi.org/10.1021/acs.nanolett.5b04840>.
- ⁵ J. Jung, A. M. DaSilva, A. H. MacDonald, and S. Adam, *Nature Communications* **6**, 1 (1), [arXiv:1403.0496](https://arxiv.org/abs/1403.0496).
- ⁶ J. Duan, X. Wang, X. Lai, G. Li, K. Watanabe, T. Taniguchi, M. Zabarjadi, and E. Y. Andrei, *Proceedings of the National Academy of Sciences* **113**, 14272 (2016), <http://www.pnas.org/content/113/50/14272.full.pdf>.
- ⁷ X. Li, S. Sundaram, Y. El Gmili, T. Ayari, R. Puybaret, G. Patriarche, P. L. Voss, J. P. Salvestrini, and A. Ougazzaden, *Crystal Growth & Design* **16**, 3409 (2016), <http://dx.doi.org/10.1021/acs.cgd.6b00398>.
- ⁸ T. Q. P. Vuong, G. Cassabois, P. Valvin, E. Rousseau, A. Summerfield, C. J. Mellor, Y. Cho, T. S. Cheng, J. D. Albar, L. Eaves, C. T. Foxon, P. H. Beton, S. V. Novikov, and B. Gil, *2D Materials* **4**, 021023 (2017).
- ⁹ D. Basov, M. Fogler, and F. G. de Abajo, *Science* **354**, aag1992 (2016).
- ¹⁰ T. Low, A. Chaves, J. D. Caldwell, A. Kumar, N. X. Fang, P. Avouris, T. F. Heinz, F. Guinea, L. Martin-Moreno, and F. Koppens, *Nature materials* **16**, 182 (2017).
- ¹¹ Y. Watanabe, W. Inami, and Y. Kawata, *Journal of Applied Physics* **109**, 023112 (2011).
- ¹² N. Mattiucci, G. D'Aguanno, H. O. Everitt, J. V. Foreman, J. M. Callahan, M. C. Buncick, and M. J. Bloemer, *Optics express* **20**, 1868 (2012).
- ¹³ J. M. McMahon, G. C. Schatz, and S. K. Gray, *Physical Chemistry Chemical Physics* **15**, 5415 (2013).
- ¹⁴ Y. Yang, J. M. Callahan, T.-H. Kim, A. S. Brown, and H. O. Everitt, *Nano letters* **13**, 2837 (2013).
- ¹⁵ G. Maidecchi, G. Gonella, R. Proietti Zaccaria, R. Moroni, L. Anghinolfi, A. Giglia, S. Nannarone, L. Mattera, H.-L. Dai, M. Canepa, *et al.*, *ACS Nano* **7**, 5834 (2013).
- ¹⁶ M. B. Ross and G. C. Schatz, *The Journal of Physical Chemistry C* **118**, 12506 (2014).
- ¹⁷ A. M. Watson, X. Zhang, R. Alcaraz de La Osa, J. M. Sanz, F. González, F. Moreno, G. Finkelstein, J. Liu, and H. O. Everitt, *Nano letters* **15**, 1095 (2015).

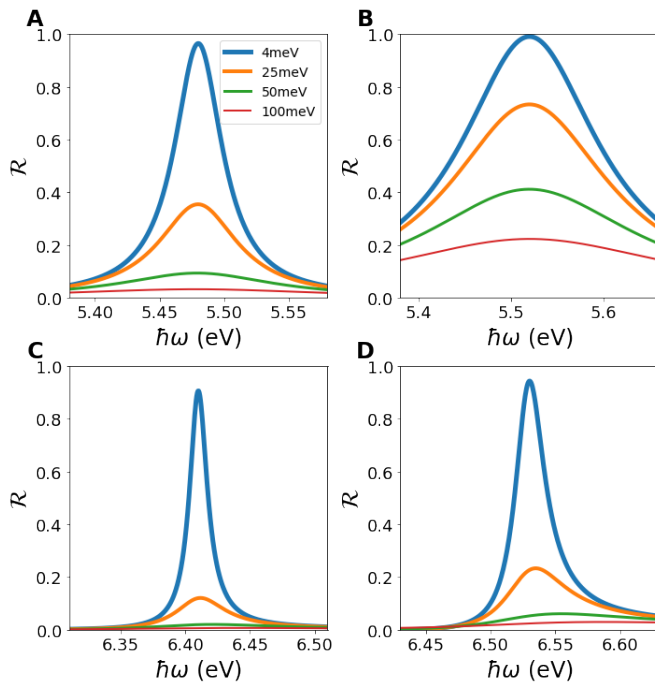


Figure 12. (Color online) Reflection coefficient for monolayer hBN and different values of $\hbar\gamma$ with the parameters from table VI. Panel (a) and (c) shows the A and B excitons, respectively, with the G_0W_0 parameters, while the panels (b) and (d) shows the result from the equation of motion formalism. As the equation of motion formalism predicts higher excitonic weights, in this case we have broader reflectance peaks around the excitons energies in comparison with the G_0W_0 result.

¹⁸ R. Alcaraz de la Osa, J. Sanz, A. Barreda, J. Saiz, F. González, H. Everitt, and F. Moreno, *The Journal of Physical Chemistry C* **119**, 12572 (2015).
¹⁹ Y. Gutierrez, D. Ortiz, J. M. Sanz, J. M. Saiz, F. Gonzalez, H. O. Everitt, and F. Moreno, *Optics express* **24**, 20621 (2016).
²⁰ Y. Gutiérrez, R. Alcaraz de la Osa, D. Ortiz, J. M. Saiz, F. González, and F. Moreno, *Applied Sciences* **8**, 64 (2018).
²¹ Y. Kumamoto, A. Taguchi, N. I. Smith, and S. Kawata, *Biomedical optics express* **2**, 927 (2011).
²² M. W. Knight, L. Liu, Y. Wang, L. Brown, S. Mukherjee, N. S. King, H. O. Everitt, P. Nordlander, and N. J. Halas, *Nano letters* **12**, 6000 (2012).
²³ A. Nagashima, N. Tejima, Y. Gamou, T. Kawai, and C. Oshima, *Physical Review B* **51**, 4606 (1995).
²⁴ L. Hedin, *Phys. Rev.* **139**, A796 (1965).
²⁵ L. Hedin and S. Lundqvist, *Solid State Physics* **23**, 1 (1970).
²⁶ E. E. Salpeter and H. A. Bethe, *Phys. Rev.* **84**, 1232 (1951).
²⁷ S. Albrecht, L. Reining, R. Del Sole, and G. Onida, *Phys. Rev. Lett.* **80**, 4510 (1998).
²⁸ X. Blase, A. Rubio, S. G. Louie, and M. L. Cohen, *Phys. Rev. B* **51**, 6868 (1995).
²⁹ H. Sahin, S. Cahangirov, M. Topsakal, E. Bekaroglu, E. Akturk, R. T. Senger, and S. Ciraci, *Phys. Rev. B* **80**, 155453 (2009).

³⁰ N. Berseneva, A. Gulans, A. V. Krasheninnikov, and R. M. Nieminen, *Phys. Rev. B* **87**, 035404 (2013).
³¹ P. Cudazzo, L. Sponza, C. Giorgetti, L. Reining, F. Sottile, and M. Gatti, *Phys. Rev. Lett.* **116**, 066803 (2016).
³² L. Wirtz, A. Marini, and A. Rubio, *Phys. Rev. Lett.* **96**, 126104 (2006).
³³ T. Galvani, F. Paleari, H. P. C. Miranda, A. Molina-Sánchez, L. Wirtz, S. Latil, H. Amara, and F. Ducastelle, *Phys. Rev. B* **94**, 125303 (2016).
³⁴ F. Ferreira and R. M. Ribeiro, *Phys. Rev. B* **96**, 115431 (2017).
³⁵ B.-C. Shih, Y. Xue, P. Zhang, M. L. Cohen, and S. G. Louie, *Phys. Rev. Lett.* **105**, 146401 (2010).
³⁶ J. A. Berger, L. Reining, and F. Sottile, *Phys. Rev. B* **82**, 041103 (2010).
³⁷ J. Deslippe, G. Samsonidze, D. A. Strubbe, M. Jain, M. L. Cohen, and S. G. Louie, *Computer Physics Communications* **183**, 1269 (2012).
³⁸ M. S. Hybertsen and S. G. Louie, *Phys. Rev. B* **34**, 5390 (1986).
³⁹ M. Rohlfing and S. G. Louie, *Phys. Rev. B* **62**, 4927 (2000).
⁴⁰ P. Giannozzi, S. Baroni, N. Bonini, M. Calandra, R. Car, C. Cavazzoni, D. Ceresoli, G. L. Chiarotti, M. Cococcioni, I. Dabo, A. Dal Corso, S. de Gironcoli, S. Fabris, G. Fratesi, R. Gebauer, U. Gerstmann, C. Gougousis, A. Kokalj, M. Lazzeri, L. Martin-Samos, N. Marzari, F. Mauri, R. Mazzarello, S. Paolini, A. Pasquarello, L. Paulatto, C. Sbraccia, S. Scandolo, G. Sclauzero, A. P. Seitsonen, A. Smogunov, P. Umari, and R. M. Wentzcovitch, *Journal of Physics: Condensed Matter* **21**, 395502 (19pp) (2009).
⁴¹ J. P. Perdew, K. Burke, and M. Ernzerhof, *Phys. Rev. Lett.* **77**, 3865 (1996).
⁴² H. J. Monkhorst and J. D. Pack, *Phys. Rev. B* **13**, 5188 (1976).
⁴³ A. Chaves, R. Ribeiro, T. Frederico, and N. Peres, *2D Materials* **4**, 025086 (2017).
⁴⁴ R. M. Ribeiro and N. M. R. Peres, *Phys. Rev. B* **83**, 235312 (2011).
⁴⁵ P. Cudazzo, I. V. Tokatly, and A. Rubio, *Physical Review B* **84**, 085406 (2011).
⁴⁶ Y. V. Bludov, A. Ferreira, N. Peres, and M. Vasilevskiy, *International Journal of Modern Physics B* **27**, 1341001 (2013).
⁴⁷ E. Arakawa, M. Williams, R. Hamm, and R. Ritchie, *Physical Review Letters* **31**, 1127 (1973).
⁴⁸ P. Halevi and R. Fuchs, *Journal of Physics C: Solid State Physics* **17**, 3869 (1984).
⁴⁹ A. Archambault, T. V. Teperik, F. Marquier, and J.-J. Greffet, *Physical Review B* **79**, 195414 (2009).
⁵⁰ M. Conforti and M. Guasoni, *JOSA B* **27**, 1576 (2010).
⁵¹ I. B. Udagedara, I. D. Rukhlenko, and M. Premaratne, *Physical Review B* **83**, 115451 (2011).
⁵² F. Cadiz, E. Courtade, C. Robert, G. Wang, Y. Shen, H. Cai, T. Taniguchi, K. Watanabe, H. Carrere, D. Lagarde, *et al.*, *Physical Review X* **7**, 021026 (2017).
⁵³ P. Back, S. Zeytinoglu, A. Ijaz, M. Kroner, and A. Imamoglu, *Physical Review Letters* **120**, 037401 (2018).
⁵⁴ G. Scuri, Y. Zhou, A. A. High, D. S. Wild, C. Shu, K. De Greve, L. A. Jauregui, T. Taniguchi, K. Watanabe, P. Kim, *et al.*, *Physical Review Letters* **120**, 037402 (2018).
⁵⁵ P. A. D. Gonçalves and N. M. R. Peres, *An Introduction to Graphene Plasmonics* (World Scientific, 2016).

⁵⁶ A. S. Rodin, A. Carvalho, and A. H. Castro Neto, *Phys. Rev. B* **90**, 075429 (2014).

Appendix A: Equation of motion formalism

The total hamiltonian that we consider in the equation of motion approach is $H = H_0 + H_I + H_{ee}$ where we have the Dirac hamiltonian:

$$H_0(\mathbf{k}) = \hbar v_F (\boldsymbol{\sigma} \cdot \mathbf{k} + \sigma_3 m v_F^2), \quad (\text{A1})$$

the dipole interaction hamiltonian:

$$\hat{H}_I(t) = -e\mathcal{E}(t)\hat{x}, \quad (\text{A2})$$

and the electron-electron interaction:

$$\hat{H}_{ee} = -\frac{e}{2} \int d\mathbf{r}_1 d\mathbf{r}_2 \hat{\psi}^\dagger(\mathbf{r}_1) \hat{\psi}^\dagger(\mathbf{r}_2) V(\mathbf{r}_1 - \mathbf{r}_2) \hat{\psi}(\mathbf{r}_2) \hat{\psi}(\mathbf{r}_1), \quad (\text{A3})$$

where we used the field operator:

$$\hat{\psi}(\mathbf{r}, t) = \frac{1}{L} \sum_{\mathbf{k}, \lambda} \phi_\lambda(\mathbf{k}) \hat{a}_{\mathbf{k}\lambda}(t) e^{-i\mathbf{k} \cdot \mathbf{r}}, \quad (\text{A4})$$

with the eigenvector of H_0 :

$$\phi_\lambda(\mathbf{k}) = \sqrt{\frac{E_k + \lambda m}{2E_k}} \begin{pmatrix} 1 \\ \frac{k_x - ik_y}{\lambda E_k + m} \end{pmatrix}, \quad (\text{A5})$$

and eigenvalues:

$$E_k = \sqrt{k^2 + m^2}. \quad (\text{A6})$$

We note that the electron-electron interaction for charges confined in a 2D material is given by the Keldysh potential:^{45, 56}

$$V(q) = -\frac{e}{2\varepsilon_0} \frac{1}{q(r_0 q + \varepsilon_m)}, \quad (\text{A7})$$

The expected value of the polarization operator for the 2D Dirac equation can be written as:

$$P(\omega) = -\frac{ig_s e}{2} \sum_{\mathbf{k}, \lambda} d_{-\lambda}(\mathbf{k}) p_\lambda(\mathbf{k}, \omega), \quad (\text{A8})$$

$g_s = 4$ takes into account the spin and valley degeneracy, $\lambda = \pm$ labels the valence (-) or the conduction (+) band. The dipole matrix element $d_{-\lambda}(\mathbf{k})$ is:

$$d_\lambda(\mathbf{k}) = -\frac{1}{2E_k} \left(\sin \theta + i \frac{m}{E_k} \cos \theta \right). \quad (\text{A9})$$

The interband transition amplitude is defined as:

$$p_\lambda(\mathbf{k}, \omega) = \int_{-\infty}^{\infty} \frac{d\omega'}{2\pi} e^{-i\omega' t} \langle \hat{a}_{\mathbf{k}, \lambda}^\dagger(t) \hat{a}_{\mathbf{k}, -\lambda}(t) \rangle. \quad (\text{A10})$$

where $\hat{a}_{\mathbf{k}, \lambda}^\dagger(t) (\hat{a}_{\mathbf{k}, \lambda}(t))$ is the creation (annihilation) operator in band λ in the Heisenberg picture.

As explained in Ref. 43, from the equation of motion for the transition amplitude we can derive the following Bethe-Salpeter Equation:

$$(\omega - \tilde{\omega}_{\lambda\mathbf{k}}) p_\lambda(\mathbf{k}, \omega) = (\mathcal{E}_0 d_\lambda(\mathbf{k}) + \mathcal{B}_{\mathbf{k}\lambda}(\omega)) \Delta f_{\mathbf{k}}, \quad (\text{A11})$$

where $\tilde{\omega}_{\lambda\mathbf{k}}$ is the renormalized transition energy:

$$\tilde{\omega}_{\lambda\mathbf{k}} = 2\lambda E_k + \lambda \Sigma_{\mathbf{k}, \lambda}^{\text{xc}}, \quad (\text{A12})$$

where the exchange self-energy is included as

$$\Sigma_{\mathbf{k}, \lambda}^{\text{xc}} = \int \frac{d\mathbf{q}}{(2\pi)^2} V(q) \Delta f_{\mathbf{k}-\mathbf{q}} [F_{\lambda' \lambda \lambda \lambda'}(\mathbf{k}, \mathbf{k} - \mathbf{q}) - F_{\lambda \lambda \lambda \lambda}(\mathbf{k}, \mathbf{k} - \mathbf{q})] \quad (\text{A13})$$

where $F_{\lambda_1 \lambda_2 \lambda_3 \lambda_4}$ are defined in Eq. (A15). We define $\Delta f_{\lambda k} = n_F(\lambda E_k) - n_F(-\lambda E_k)$ where n_F is the Fermi-Dirac distribution and which gives us the difference in occupation between valence and conduction bands for a vertical transition. Finally, the integral term $\mathcal{B}_{\mathbf{k}\lambda}(\omega)$ is:

$$\mathcal{B}_{\mathbf{k}\lambda}(\omega) = \int \frac{d\mathbf{q}}{(2\pi)^2} V(|\mathbf{k} - \mathbf{q}|) [p_\lambda(\mathbf{q}, \omega) F_{\lambda' \lambda' \lambda \lambda}(\mathbf{k}, \mathbf{q}) + p_{\lambda'}(\mathbf{q}, \omega) F_{\lambda' \lambda \lambda' \lambda}(\mathbf{k}, \mathbf{q})] \quad (\text{A14})$$

The homogeneous part of equation A11, obtained by setting $\mathcal{E}_0 = 0$, can be used to calculate the excitons wavefunctions and energies. From the inhomogeneous solution of A11, $p_\lambda(\mathbf{k}, \omega)$ the macroscopic polarization $P(\omega)$ can be calculated using Eq. A8 and from there it follows the optical conductivity, permittivity and absorbance.

The overlap of four wavefunctions is given by the $F_{\lambda_1, \lambda_2, \lambda_3, \lambda_4}(\mathbf{k}_1, \mathbf{k}_2)$ function:

$$F_{\lambda_1, \lambda_2, \lambda_3, \lambda_4}(\mathbf{k}_1, \mathbf{k}_2) = \phi_{\lambda_1}^\dagger(\mathbf{k}_1) \phi_{\lambda_2}(\mathbf{k}_2) \phi_{\lambda_3}^\dagger(\mathbf{k}_2) \phi_{\lambda_4}(\mathbf{k}_1). \quad (\text{A15})$$

Appendix B: Exciton in the polariton electrostatic limit

In the electrostatic limit the TM exciton-polariton equation read as:

$$\frac{\varepsilon_1 + \varepsilon_2}{q} + i \frac{\sigma(\omega)}{\varepsilon_0 \omega} = 0, \quad (\text{B1})$$

with the solution:

$$\hbar\omega(q) = E_n + \frac{M_n}{\frac{(\varepsilon_1 + \varepsilon_2)b_n}{4\pi\alpha c q} + 1} b_n - i\hbar\gamma, \quad (\text{B2})$$

where b_n can be a complex quantity, the polariton lifetime is given by $-1/\Im[\omega]$, and:

$$\Im[\omega] = -\gamma - \frac{1}{\hbar} \frac{M_n \Im[b_n]}{\left| \frac{(\varepsilon_1 + \varepsilon_2)b_n}{4\pi\alpha c q} + 1 \right|^2}, \quad (\text{B3})$$

from (B2) we can see that excitons-polaritons always exist in TMD's systems. For the parameters considered, $\Re \left[\frac{M_n}{\frac{(\varepsilon_1 + \varepsilon_2)b_n}{4\pi\alpha c q} + 1} b_n \right] > 0$, so the exciton-polariton will al-

ways exists for energies higher than the exciton energy. This term also defines the exciton-polariton bandwidth, for $q \rightarrow \infty$:

$$\Re [\hbar\omega(q \rightarrow \infty)] = E_n + M_n \Re [b_n]. \quad (\text{B4})$$